Microwave Radiometer MTVZA-GY on New Russian Satellite Meteor-M No. 2-2 and Sudden Stratospheric Warming Over Antarctica

Leonid M. Mitnik, *Fellow, IEEE*, Vladimir P. Kuleshov, Maia L. Mitnik, Grigory M. Chernyavsky, Igor V. Cherny, and Andrey M. Streltsov

***Abstract*—The Meteor-M No. 2-2 meteorological satellite with the microwave radiometer MTVZA-GY on board was launched into a circular sun-synchronous orbit on July 5, 2019. The radiometer conducts a conical scanning at 65-degree incidence angle and receives the Earth's outgoing radiation in the frequency range $\nu \approx$ 6–190 GHz. The swath width is 2500 km on ascending orbits and 1500 km on descending orbits. The parameters of the ocean, land surface, and troposphere are extracted from brightness temperatures $T_B(\nu)$ measured at imager frequencies of 6.9, 10.65, 18.7, 23.8, 31.5, 36.5, 42, 48, and 91.65 GHz in vertical and horizontal polarizations. Measurements at the sounder frequencies (ten channels in the 52–58 GHz oxygen absorption band and three channels in the strong water vapor resonance line region centered at 183.31 GHz) provide information on air temperature and humidity in the troposphere and stratosphere. The structure and development of dynamic atmospheric phenomena of synoptic scale are imprinted on the global $T_B(\nu)$ maps at imager frequencies. The $T_B(\nu)$ time series at the sounder frequencies allowed us to detect and trace the evolution of a rare phenomenon — a sudden stratospheric warming over Antarctica in August–September 2019.**

***Index Terms*—Atmospheric measurements, cyclones, deep convection, microwave (MW) radiometry, remote sensing, sea ice, sudden stratospheric warming (SSW).**

I. Introduction

The Russian polar-orbiting meteorological satellite Meteor-M No. 2-2 with a scanning microwave (MW) radiometer MTVZA-GY on board was launched into a circular 832-km sun-synchronous orbit on July 5, 2019 [1]. The customer, Roscomgidromet, accepted the satellite into operation in November 2019 after the end of the test period. The local time of crossing the equator on ascending node is 15:00. The radiometer continues the global measurements of outgoing MW radiation from the ocean, land cover, sea ice, and atmosphere performed in 2014–2017 from Meteor-M No. 2 satellite [2].

MTVZA-GY receives the Earth's outgoing radiation at 22 frequencies ν in the 6.9–190 GHz range, thus integrating the functions of imager and sounder. The conical scanning at the incidence angle of $\theta = 65°$ provides the swath width of 2500 km in ascending orbits. In descending orbits, the inclination of the solar cells changes, which leads to a partial shadowing of the swath and reducing its width to 1500 km [1]. Multichannel MW measurements are the basis for simultaneous estimation of key geophysical parameters of the underlying surface (temperature T_0, emissivity $\kappa(\nu)$, etc.) and atmosphere (total water vapor content V, total cloud liquid water content Q, etc., over the ocean). The global data of the MW sensing visualize the structure of the marine weather systems and allow us to monitor their evolution, the variability of the air circulation, and temperature in the troposphere and stratosphere [3].

This work investigates the global brightness temperature fields at frequencies in the range of 6.9–190 GHz with vertical (V) and horizontal (H) polarizations $T_B{}^{V,H}(\nu)$. The transition from the measured antenna temperatures to the brightness temperatures is performed according to the external calibration data. The hot reference region is the Amazon rainforest. The cold reference region was chosen over the cloudless ocean areas with weak winds and low values of atmospheric water vapor content around Antarctica. The brightness temperatures over the reference regions were determined by numerical integration of the MW radiative transfer equation in the underlying surface–atmosphere system [1], [2].

The values of $T_B{}^{V,H}(\nu)$ at the imager frequencies ν = 6.9, 10.65, 18.7, 23.8, 31.5, 36.5, 42, 48, and 91.65 GHz depend on both the surface and atmospheric parameters. The $T_B{}^{V,H}(\nu)$ fields give an insight into the spatial structure and variability of the parameters of tropical, extratropical, and polar cyclones;, fronts; intertropical convergence zone (ITCZ); atmospheric rivers; cold air outbreaks; and other weather systems [1], [2].

The air temperature in the middle troposphere–stratosphere is determined by measurements at ten frequencies in the 52–58 GHz range on the long-wave slope of the strong oxygen absorption band, and the air humidity characteristics are determined by observations at three frequencies near 183.3 GHz and at 23.8 GHz.

Manuscript received May 31, 2021; revised September 2, 2021, October 26, 2021, and November 28, 2021; accepted November 29, 2021. Date of publication December 9, 2021; date of current version January 12, 2022. This work was supported by the Russian Science Foundation under Grant 20-17-00179. *(Corresponding author: Leonid M. Mitnik.)*

Leonid M. Mitnik, Vladimir P. Kuleshov, and Maia L. Mitnik are with the Satellite Oceanology Department, V. I. Il'ichev Pacific Oceanological Institute, FEB RAS, 690041 Vladivostok, Russia (e-mail: lm_mitnik@mail.ru; 986022@mail.ru; maia_mitnik@mail.ru).

Grigory M. Chernyavsky, Igor V. Cherny, and Andrey M. Streltsov are with the JSC Russian Space Systems, 117997 Moscow, Russia (e-mail: icherny@space.ru; cherny1@space.ru; cherny2@space.ru).

Digital Object Identifier 10.1109/JSTARS.2021.3133425

TABLE I
SOUNDER CHANNELS CHARACTERISTICS

Channel marking	Central frequency [GHz]	Bandwidth [MH]	NEDT [K/pixel]	Height of WF maximum [km]
O1	52.80	400	0.4	2
O2	53.30	400	0.4	4
O3	53.80	400	0.4	6
O4	54.64	400	0.4	10
O5	55.63	400	0.4	14
O6	$\nu_0 \pm 0.1$	50	0.4	20
O7	$\nu_0 \pm 0.05$	20	0.7	25
O8	$\nu_0 \pm 0.025$	10	0.9	30
O9	$\nu_0 \pm 0.01$	5	1.3	35
O10	$\nu_0 \pm 0.005$	3	1.7	42
HO1	183.31 ± 7.0	1500	0.5	1.5
HO2	183.31 ± 3.0	1000	0.6	2.9
HO3	183.31 ± 1.4	500	0.8	4.7

$\nu_0 = 57.2903 \pm 0.3222$ GHz, WF — weighting function

The results of MTVZA-GY observations on a board of Meteor-M No. 2 were in good agreement with the measurements of AMSR2 and GMI radiometers at coincident or nearby frequencies 10.65, 18.7, 23.8, 36.5, 89 GHz and near 183.3 GHz, with the products retrieved from MW radiometer data, as well as with visible and infrared satellite images, radiosonde data, weather maps, etc. [2]–[5].

II. MTVZA-GY RADIOMETER AND DATA

Continuous observations of the Earth's outgoing radiation by the Meteor-M No. 2-2 MTVZA-GY radiometer began on August 6, 2019. The effective field of view (EFOV) of the radiometer antenna varies from 133×297 km at $\nu = 6.9$ GHz to 14×30 km at 91.65 GHz and to 9×14 km at 183.3 GHz [2]. The pixel size is 32×32 km for 6.9 to 48 GHz and near 183.3 GHz channels, 10×16 km at 91.65 GHz, and 48×48 km on all ten oxygen channels [1], [2]. The noise equivalent differential temperature (NEDT) was derived for the EFOV after averaging several pixels together. It was then converted to a single pixel or instantaneous field of view based on an integration time of 30 ms and a scene temperature of 300 K. The NEDT value of the imager channels is 0.3–0.6 K/pixel and that of the sounder channels is 0.4–1.7 K/pixel [1], [2]. The sounder channel characteristics are given in Table I.

The MTVZA-GY receivers are total power radiometers, which view hot/cold calibration targets once per scan. Scan period is equal to 2.5 s. The hot target calibration is MW absorber (black-body) with temperature of 235–250 K, which is measured by means of four platinum thermistors [1]. The cold target calibration is performed by a small reflector that receives the cosmic relic radiation. This occurs at an antenna azimuth position of 45° (looking forward and to the right-hand side of the satellite track), while the main reflector simultaneously views the Earth's surface [1], [2].

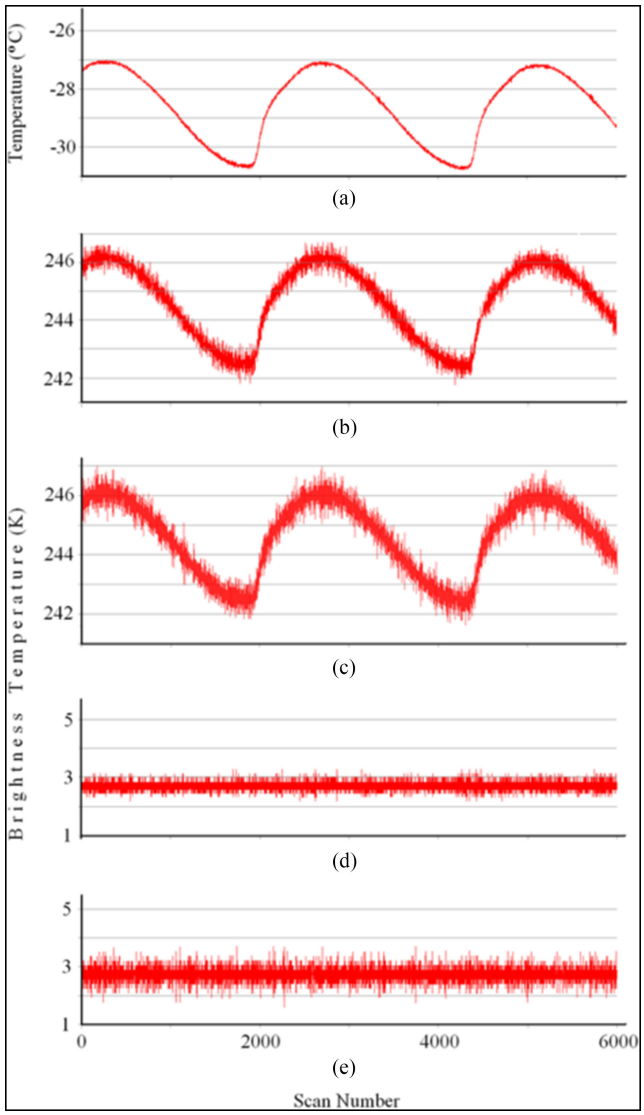

Fig. 1. Calibration of 10.65 and 183.31 ± 7 GHz channels on the radiation of the hot and cold targets at 452–454 turns in August 2019. (a) Physical temperature. (b)–(e) Brightness temperature of hot (a) and (b) and cold (d) and (e) targets at 10.65 GHz (b) and (d) and at 183.31 ± 7 GHz (c) and (e), correspondingly.

Fortunately, at MW frequencies, space is a homogeneous, isotropic distributed target of constant brightness 2.73 K. This greatly simplified the radiometric calibration procedure by not requiring an adjustment in the observed brightness temperature depending on the viewing direction. Space provides a uniform brightness temperature of 2.73 K with a variation of less than 100 μK about the Galactic plane.[1]

As an example, Fig. 1 shows the radiometric measurements of hot and cold calibration targets in the 10.65 and 183.31 ± 7 GHz channels from the 452 to 454 turns in August 2019. The changes

[1] [Online]. Available: http://aether.lbl.gov/www/projects/cobe/COBE_home/cobe_home.html

of physical temperature of hot black body were from –27 to –31 °C [see Fig. 1(a)], which corresponds to the changes of its brightness temperature accordingly from 246 to 242 K [see Fig. 1(b) and (c)]. Meanwhile, the level of cold target brightness temperature was a constant, although the beam of calibration antenna crossed the celestial sphere three times [see Fig. 1(d) and (e)].

The internal calibration provides an absolute scale of antenna temperatures for all MTVZA-GY channels, which is related to the cosmic relic radiation of 2.73 K. It follows that the MW radiometric measurements should be characterized as stable. The standard deviation of the black body brightness temperature in the 10.65 GHz is 0.21 K and in 183.31 ± 7 GHz channel is 0.37 K for an integration time of 30 ms (Fig. 1), which corresponds to a sensitivity of 0.26 and 45 K, correspondingly.

The external calibration of the imager channels was performed using measurements of the outgoing radiation of hot zones in the Amazon rainforest and cold ocean regions around Antarctica and to the west of South America, which were distinguished by histograms. The position and sizes of these zones and the minimum values of the signals (counts) $n^{V,H}(\nu)$ recorded in them varied from day to day depending on the near surface wind speed W, cloud liquid water content Q, and total atmospheric water vapor content V.

Areas with low counts and an area >35 000 km^2, identified by processing measurements over five to seven days, were chosen for calibration. A joint analysis of the count fields at frequencies 10.65, 23.8, and 42 GHz with H-polarization having different sensitivity to variations of Q, V, and W parameters allows one to select cloudless zones with minimal atmospheric water vapor content and weak winds, which reduces the calibration errors. The errors also decrease when selecting zones with a larger area due to smoothing the parameter variations.

The emissivity of the flat ocean surface $\kappa^{V,H}(\nu,\theta)$ was found using the Fresnel formulas. The dependencies of the real and imaginary parts of the dielectric permittivity of water on frequency, temperature T_0, and salinity S_0, obtained by generalization of a large array of experimental data, were used [6], [7]. At $\theta = 65°$, the T_0 dependences of the brightness temperature of a flat (at $W = 0$ m/s) ocean surface $T_{B0} = T_0 \times \kappa^{V,H}(\nu, \theta)$ at MTVZA-GY imager frequencies are shown in Fig. 2. T_{B0} values at several frequencies with H- and V-polarizations are weakly dependent on water temperature. Thus, at $\nu = 10.65$ GHz, T_{B0} variations in H-polarization do not exceed 0.2 K when T_0 changes from –1.5 to +11 °C, T_{B0} variations in V-polarization at $\nu = 23.8$ and 36.5 GHz lie within 1 K, when T_0 changes from 4 to +14 °C and from 8 to +18 °C, respectively. The weak dependences of T_{B0} on T_0, and the inertia of the temperature field of the ocean are the important features that reduce the requirements to the accuracy of the SST setting. Therefore, it is possible to take SST values averaged over several days or a week before calibration.

The dependencies $\kappa^{V,H}(\nu, T_0)$ and ${T_{B0}}^{V,H}(\nu, T_0)$ are well approximated by second-order polynomials, which are used in the algorithms for the recovery of W, Q, and V parameters

$$ {T_{B0}}^{V,H}(\nu) = {b_0}^{V,H}(\nu) + {b_1}^{V,H}(\nu)\, T_0 + {b_2}^{V,H}(\nu)\, {T_0}^2. $$

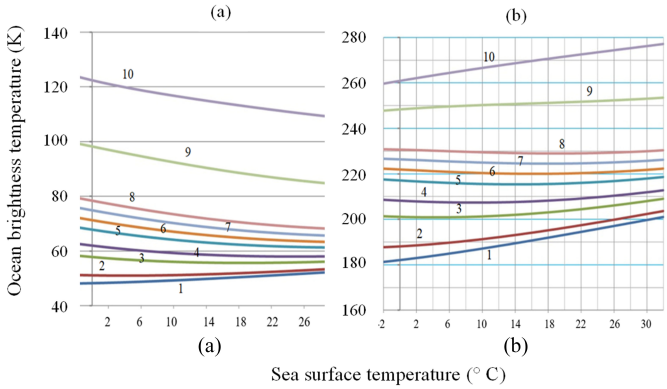

Fig. 2. Dependences of the brightness temperature with the (a) horizontal and (b) vertical polarizations of the flat ocean surface on the water surface temperature at $S_0 = 35\%$ and $\theta = 65°$. The digits correspond to the radiometer frequencies: 1 – 6.9, 2 – 10.65, 3 – 18.7, 4 – 23.8, 5 – 31.5, 6 – 36.5, 7 – 42, 8 – 48, 9 – 91.65; and 10 – 176.3 GHz.

TABLE II
COEFFICIENTS OF APPROXIMATION FORMULA

Frequency [GHz]	${b_0}^{H}$ [K]	${b_1}^{H}$	${b_2}^{H}$
10.65	51.142	–0.02051	0.003495
18.7	57.831	–0.22864	0.005903
23.8	61.991	–0.32845	0.007370
31.5	67.832	–0.43969	0.006727
36.5	71.452	–0.49444	0.007551
42.0	74.886	–0.53728	0.007595
48.0	78.488	–0.57343	0.007530

Coefficients of the above formula at several imager frequencies at horizontal polarization are given in Table II.

To reduce calibration errors, hot spots in the Amazonian rainforest were selected by the joint analysis of the sampling fields at several frequencies, which allows filtering out areas with less dense vegetation, increased cover moisture, and/or open water patches (from data at 10.65 GHz), with thick cloud cover (from data at 42 GHz) and deep convection (from data at 91.65 and 183.31 ± 7 GHz). Satellite visible and infrared images were used to confirm the presence of clouds. As in the cold calibration, preference was given to sites where meteorological and radiosonde stations were available.

The emissivity of dense forest cover was taken from [8], and its surface temperature was taken from the readings of the nearest meteorological stations. In the absence of clouds, the surface temperature was estimated from the counts of satellite infrared radiometers, which is necessary to account for its diurnal variations.

$T_B(\nu)$ over the ocean and land were calculated by numerical integration of the equation of MW radiation transfer in the atmosphere–underlying surface system [1]–[3], [9]. The vertical profiles of atmospheric pressure, temperature, and humidity were taken from radiosonde data at the stations closest to the chosen calibration regions [10] or from model data for the corresponding latitude belt and season [11].

The errors in the calculated $T_B(\nu)$ depend on the frequency and polarization and can be 2–4 K, which are due to the lack of

regular *in situ* measurements and inaccuracy of the description of MW radiation transfer in the atmosphere–underlying surface system.

The $T_B(\nu)$ were compared with the measured counts over the hot and cold regions. As a result, the calibration coefficients in the equation linking the $T_B(\nu)$ with the counts were determined for each channel. The same procedures were made regularly to monitor radiometer operation in space and estimate its contribution into $T_B(\nu)$ variations.

The stability of the radiometer functioning in flight was determined by analyzing the difference of the time series of the brightness temperatures $T_B(\nu)$ averaged over uniform circular regions with an area greater than 35 000 km^2, obtained by MTVZA-GY and AMSR2 at the same frequencies and polarizations. AMSR2 data were considered as reference ones. The following areas were chosen for the external calibration: Near Amazon Tall Tower Observatory (ATTO) (2.15° S, 59.00° W) and Zotino Tall Tower Observatory (ZOTTO) (60.80° N, 89.35° E) in the Krasnoyarsk Territory (Russia), in Antarctica near Concordia station (75.10° S, 123.35° E), and in Greenland near Summit station (72.57° N, 38.45° W).

Measurements of MTVZA-GY stopped on December 18, 2019, after the satellite collided with a micrometeorite, which caused satellite depressurization and changes in the thermal regime. Control power-ups of MTVZA-GY after several instruments were powered down showed that all elements of the radiometer were working normally after transition period of about seven to ten days. The global MW observations resumed at the end of January 2020. Subsequent interruptions in the instrument's operation lasting from minutes to several days were caused both by technical reasons (malfunction of the analog/digital convertor) and by external factors (impact of high energy cosmic particles). Such events were observed when the satellite flew over the South Atlantic, where the Earth's magnetic field is minimal [12]. Estimates after these interruptions show that most of the MTVZA-GY channels continue to operate stably.

The long-term stability of the radiometer since September 2019 to the present (October 2021) is investigated by analyzing the difference in the time series of $T_B(\nu)$ measured by the Meteor-M No. 2-2 MTVZA-GY and GCOM-W1 AMSR2 $\Delta T_B(\nu) = T_B(\nu)_{\mathrm{MTVZA\text{-}GY}} - T_B(\nu)_{\mathrm{AMSR2}}$ at frequencies $\nu = 10.65$, 18.7, 23.8, 36.5, and 91.65/89 GHz. More accurate and reliable estimates $T_B(\nu)$ were obtained for the period February 6, 2020–September 30, 2021, that is, after the depressurization of the satellite and the end of the transition period after the radiometer reactivation. For all channels, the trend of the difference $\Delta T_B(\nu)$ over the whole period (602 days) did not exceed 0.2 K. A trend of 0.32 and 0.6 K was registered at 23.8 and 36.5 GHz with vertical polarization, respectably. Possible causes of the trend could be the correction of AMSR2 calibration (calibration of MTVZA-GY was not changed), drift of the equator crossing time of the Meteor-M No. 2-2 and changes in the MTVZA-GY parameters, which requires additional studies. The same approach applied earlier to MTVZA-GY onboard Meteor-M No. 2 showed the high long-term stability of the radiometer [2], [3]. A small ($\approx$1 K/year) trend for two years was registered at $\nu = 23.8$ GHz only.

The significant $T_B(\nu)$ changes from scan to scan (striping noise) and along the scan were revealed in channels O1–O10, which complicate the interpretation of the data. Striping noise was also observed in the microwave temperature sounder (MWTS-2) radiometer on the Chinese Feng Yun (FY)-3C satellite [13]. The variation of brightness along the scan is probably due to changes in the level of rereflected signals during scanning and in the degree of shading of the antenna pattern by solar elements. Impact of these problems, as the ground experiments have shown, can be decreased by correcting the alignment, which should be implemented on the Meteor-M No. 2-3 satellite, planned to launch of in 2022.

III. MODELING

Modeling of the brightness temperatures of the Earth's outgoing radiation is necessary to develop algorithms for retrieval of geophysical parameters for the given characteristics of radiometer and sensing geometry [9], [14]–[17], to perform radiometer calibration [2], [18] and to assess its functioning in flight, as well as for choosing characteristics of promising radiometers and satellites [2], [3].

The input data for calculating the brightness temperatures of the outgoing radiation of the atmosphere–underlying surface system $T_B{}^{V,H}(\nu)$ consist of the radiosonde (*r/s*) profiles of atmospheric pressure $P(h)$, temperature $T(h)$, and relative humidity $u(h)$, profiles of cloud liquid water content $\omega(h)$, the values of emissivity $\kappa(\nu, \theta)$, and the surface temperature T_S of different types of land [8], sea ice [19], [20], and Antarctic and Greenland ice sheets [21]–[24]. For the ocean, the input data include temperature T_0 and salinity S_0 of the water surface and the near surface wind speed W. *r/s* data are freely available at Wyoming University [10], and $\omega(h)$ profiles are constructed from $u(h)$ and $T(h)$ profiles and experimental data on the liquid water content of different cloud types [25].

When modeling $T_B{}^{V,H}(\nu)$ over the ocean, the emissivity $\kappa^{V,H}(\nu, \theta)$ are found from the values of dielectric permittivity of saline water [6], given parameters ν, T_0, S_0, and wind speed W, and empirical dependences of increments of $\Delta\kappa^{V,H}(\nu, \theta)$, caused by wind action [7].

The spectra of brightness temperature with *V*- and *H*-polarizations over the ocean under weak wind (2 m/s) and in the absence of clouds are shown in Fig. 3. The calculations are based on ship radiosonde data for the polar and tropical atmospheres [9].

Fig. 4 shows the simulated spectra of the brightness temperatures over the polar ocean in clear skies (1 and 3) and in clouds with total liquid water content of 0.17 kg/m^2 (2 and 4) and over sea ice with emissivity of 0.6 (5) and 0.8 (6). Calculations were made from radiosonde profiles of pressure, temperature, and relative humidity measured at 00 UTC on 24 September 2019 at station 89571 Davis (68.57° S, 77.9° E, altitude 22 m) at a surface air temperature of –7.9 °C.

IV. GLOBAL FIELDS OF BRIGHTNESS TEMPERATURE

The global MTVZA-GY data from Meteor-M No. 2-2 satellite was acquired for the period from August 6, 2019 to September 30, 2021 (at the time of article revision). When measured over

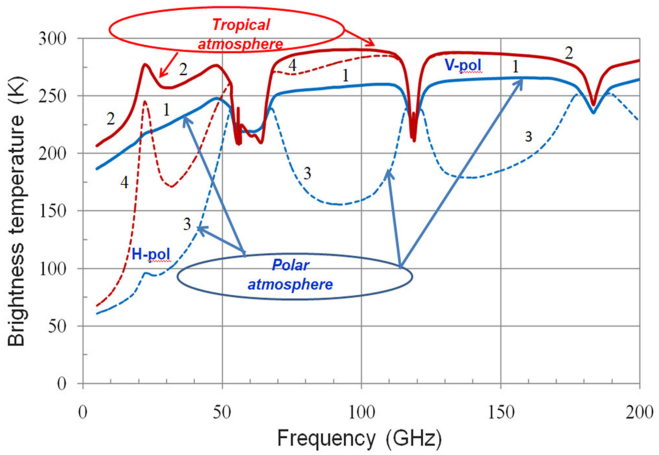

Fig. 3. Spectra of brightness temperatures over the ocean on vertical (solid lines 1, 2) and horizontal (dashed lines 3, 4) polarizations calculated from ship radiosonde data at incident angle $\theta = 65°$ and $W = 2$ m/s for cloudless polar (SST = 3.7 °C, $V = 3.7$ kg/m^2) (blue lines 1 and 3) and tropical (SST = 30.8 °C, $V = 51$ kg/m^2) (red lines 2 and 4) atmospheres.

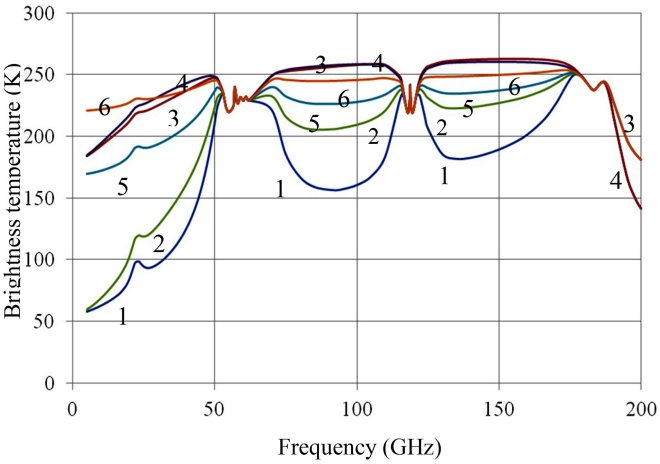

Fig. 4. Spectra of simulated brightness temperatures with horizontal (blue line 1, green line 2) and vertical (3, 4) polarizations over the polar ocean in clear skies (blue line 1 and 3) and cloud cover with a total liquid water content of 0.17 kg/m^2 (green line 2 and 4) and over the ice cover with emissivity 0.6 (light blue line 5) and 0.8 (orange line 6).

the ocean at 10.65 GHz with H-polarization, liquid precipitation and clouds are characterized by higher brightness temperature $T_B(10H)$. They appear as bands and spots which give idea about spatial structure of the various weather systems [see Fig. 5(a)]. However the increase of $T_B(10H)$ is also due to the increase in the emissivity of the sea surface under wind action [7], [14], [16], [17]. In order to isolate the increments due to wind and cloudiness, the upper limit of $T_B(10H)$ was taken to be 110 K. As a result, the wind variability is reliably recorded in the vicinity of atmospheric fronts in the extratropical and tropical cyclones and atmospheric rivers in both hemispheres, in the ITCZ in the Pacific, Atlantic, and Indian Oceans, while the land covers, sea ice, Antarctica, and Greenland ice sheets, whose brightness temperature is much higher than 110 K, are displayed in Fig. 5(a) with a uniform brown tone.

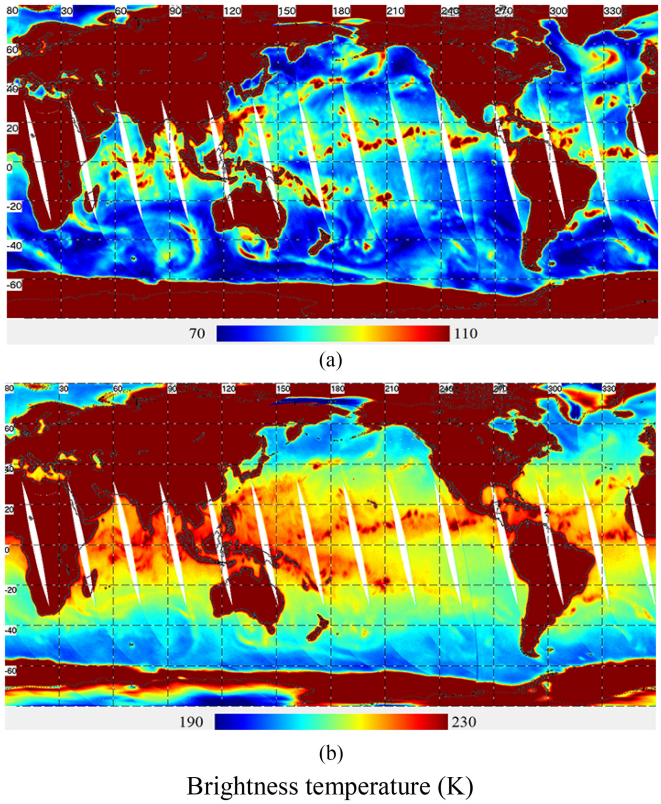

Fig. 5. Brightness temperature of the Earth at 10.65 GHz with the (a) horizontal and (b) vertical polarizations as measured by the MTVZA-GY on the ascending orbits on November 11, 2019.

The contribution of the wind to the T_B variations in the V-polarization is much smaller than the horizontal one, but the influence of SST is clearly pronounced, as evidenced by the growth of $T_B(10V)$ in the tropical and subtropical ocean regions, where $T_0 \geq 20$ °C [see Fig. 5(b)], which agrees with the model results (Fig. 2(b), curve 2).

The upper limit of $T_B(10V)$ was taken to be 230 K, and therefore the brightness temperature variations over the continents are not visible. The brightness temperature of the sea ice around Antarctica is higher than 230 K, and the ice sheets of Greenland and Antarctica are lower than 230 K due to the low temperature of the effectively radiating layer of ≈50 m thickness [24].

The sensitivity of brightness temperatures to the variations in atmospheric water vapor content V and in cloud liquid water content Q is increased with frequency. In the T_B fields at frequencies 23.8, 31.5, 36.5, 42, and 48 GHz, the gradients of V and Q are brightly manifested and regions of high atmospheric water vapor content, power cloudiness, and precipitation in the tropical zone, in extratropical cyclones and polar lows of both hemispheres are clearly distinguished (see Figs. 6 and 7). The V values in the tropical zone reach 55–60 kg/m^2 and more and in the Southern Ocean around the sea ice belt surrounding Antarctica are 3–10 kg/m^2. The V values are also noticeably higher than the background values in atmospheric rivers, a narrow corridor or filament of concentrated moisture in the atmosphere, which is a characteristic feature of atmospheric circulation in both

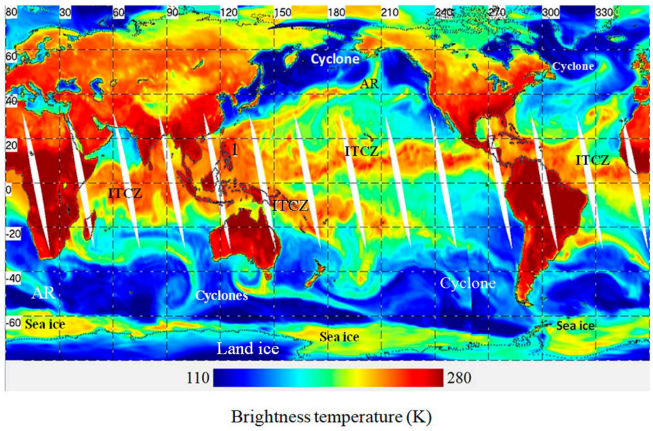

Fig. 6. Brightness temperature of the Earth at 23.8 GHz with horizontal polarization as measured by MTVZA-GY on November 11, 2020. ITCZ – intertropical convergence zone, 1 – typhoon Vamco, AR – atmospheric river.

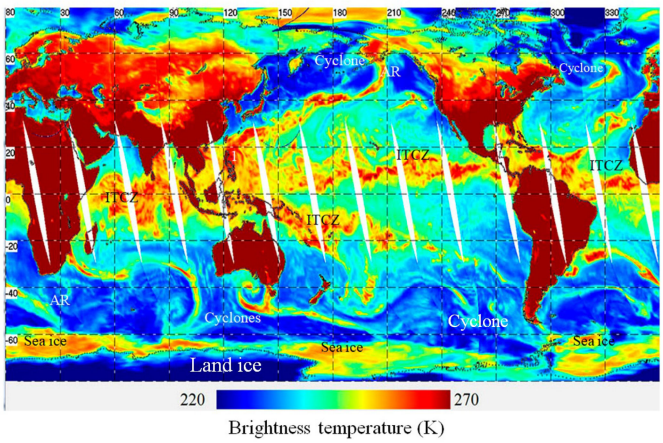

Fig. 7. Brightness temperature of the Earth at 42 GHz with horizontal polarizations on November 11, 2020. 1 – typhoon Vamco, AR – atmospheric river, ITCZ – intertropical convergence zone.

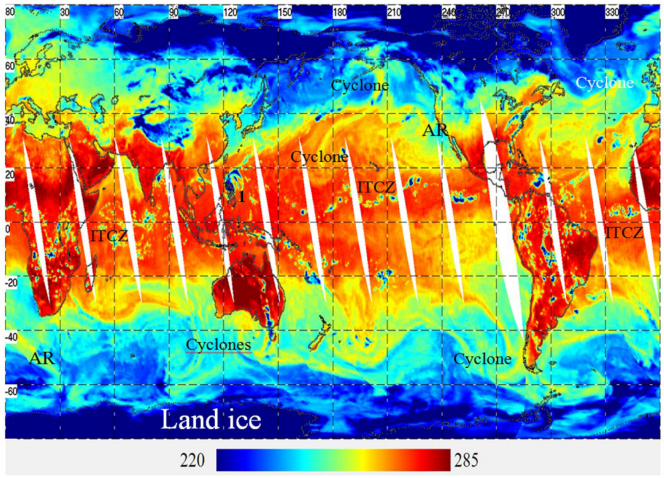

(a)

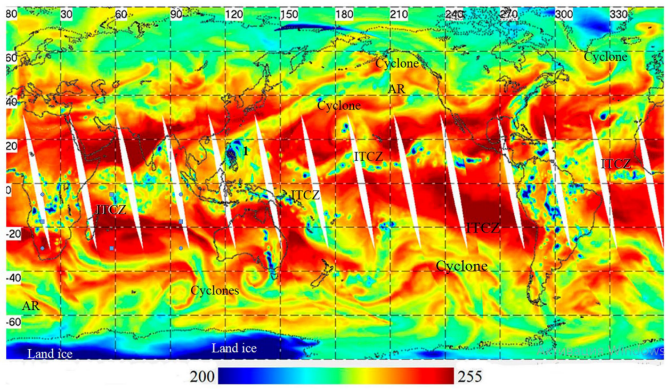

(b)

Fig. 8. Global brightness temperature at (a) 91.65 GHz and (b) 183.31 ± 1.4 GHz with vertical polarization as measured by MTVZA-GY on November 11, 2020. 1 – typhoon Vamco, AR – atmospheric river, ITCZ – intertropical convergence zone.

hemispheres [26], [27]. The influence of V on $T_B(\nu)$ is most noticeable at $\nu = 23.8$ GHz (Fig. 6).

Atmospheric fronts of synoptic-scale cyclones, where cloud liquid water content values increase to 0.5–1 kg/m^2 and more and precipitation falls are clearly visualized in the fields of brightness temperatures $T_B(36H)$ and $T_B(42H)$ (Fig. 7). The effects of increased absorption in clouds and precipitation and improved resolution are more noticeable than at lower frequencies, which follow from comparison of Figs. 6 and 7 and the results of numerical experiments. Details in the structure of atmospheric cyclones, typhoon Vamco (1) and ITCZ cloudiness that were not detected in the T_B fields at lower frequencies became visible. A better indication of cloudiness and precipitation is also facilitated by the choice of the minimum and maximum values of the brightness temperatures. This choice also provides a better indication of the T_B variations over land, caused by changes in the surface temperature and emissivity.

With increasing frequency, the brightness temperature of the atmosphere and surface depends to an increasing degree on scattering of radiation on particles: Raindrops, hail, and watered hail and snow (firn). Scattering causes a decrease of T_B especially on V-polarization. From the joint analysis of the T_B fields in Figs. 5–8 and synoptic weather maps follows that precipitation over the ocean and over land (in equatorial Africa, on the islands of Indonesia, in Central and South America) falls in the atmospheric fronts of extratropical and tropical cyclones, in ITCZ, and atmospheric rivers.

MTVZA-GY radiometer channels show the possibility of detecting zones of deep convection in the atmosphere, which are associated with such hazards as thunderstorms, squalls, heavy rainfall, and floods. In Fig. 8, the precipitation zones are distinguished in the form of spots and extended formations, whose brightness temperature at $\nu = 91.65$ GHz and especially at $\nu = 183.31 \pm 1.4$ GHz is significantly lower than that of the background.

The imager frequencies display well the distribution of sea ice around Antarctica. The emissivity of sea ice $\kappa_{\text{ice}}(\nu)$ is much larger than that of sea water $\kappa_{\text{water}}(\nu)$, especially in horizontal polarization. Therefore, although the ice surface temperature is

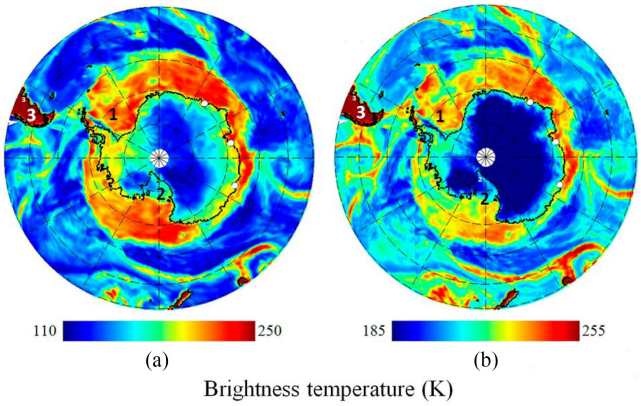

Fig. 9. Southern polar region of the Earth in winter as measured by the MTVZA-GY radiometer at (a) 23.8 GHz and at (b) 48 GHz with horizontal polarization on November 11, 2020. 1 – Weddell Sea, 2 – Ross Sea, 3 – South America.

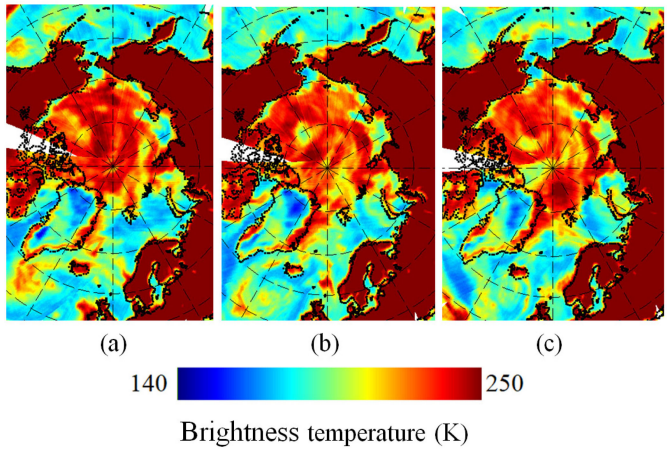

Fig. 10. MW images of Greenland and the Arctic Ocean at 42 GHz with horizontal polarization acquired on (a) June 22, (b) June 23, and (c) June 24, 2020.

less than water temperature, the satellite-measured brightness temperatures $T_B{}^H(\nu)$ of the ice are markedly higher than T_B of the ocean, as illustrated by the images of the South Polar region acquired on November 11 in Fig. 9. The brightness temperature of sea ice and shelf ice in the Weddell Sea (1) and in the Ross Sea (2) change with frequency, polarization, and season [19], [21], [23].

The minimum values of $T_B(\nu)$ are noted in East Antarctica at heights $H > 2$–3 km, where, throughout the year, the surface temperature, and the temperature of the 10-m upper firn layer, which determine the intensity of the outgoing radiation [23]–[25] are much lower than in West Antarctica.

A characteristic feature of the Southern Ocean is intensive interaction with the atmosphere, which is associated with high wind speed in cyclones that gird Antarctica all year round. The fronts in cyclones and atmospheric rivers are visualized in the brightness temperature fields recorded at the frequencies of the MTVZA-GY imager. The sensitivity of T_B to variations in wind speed, atmospheric water vapor content, and cloud liquid water content changes with frequency (Figs. 5–9), which is used in retrieval algorithms of atmospheric and ocean parameters [3], [9], [14]–[17]. Algorithms are applied in studying the atmospheric circulation, spatial structure and evolution of individual cyclones, atmospheric rivers, and cold air outbreaks. A particular relevance is the estimate of heat, moisture, and snow mass fluxes carried to Antarctica by atmospheric rivers [26], [27].

The contrasts of $T_B(\nu)$ between the inland very cold and coastal regions are also noted in Greenland (Fig. 10). The amplitude and spatial distribution of brightness contrasts are indicators of snow melting; the brightness temperature of wet snow is markedly higher than that of dry snow [28]. Melting is observed over large areas, as can be seen on the MW images of Greenland and sea ice at 42 GHz with *H*-polarization for three successive days June 22–24, 2020 (Fig. 10). Melting manifests itself in the southwestern sector of Greenland and along its east coast.

The variations in the brightness of sea ice in the Arctic Ocean are determined by ice melting and the influence of cloudy cyclones moving over the polar region (Fig. 10). The atmospheric fronts associated with the cyclone over the northern Atlantic Ocean to the south of Greenland are well distinguished due to the high cloud liquid water content and precipitation.

V. Sudden Stratospheric Warming

Shortly after the launch of the Meteor-M No. 2-2, the MTVZA-GY radiometer registered over Antarctica a sudden stratospheric warming (SSW), an extremely rare phenomenon in the Southern Hemisphere. SSW is a phenomenon in which the temperature of the polar stratosphere rises by several tens of degrees (up to 50 °C) in a few days [29], [30]. The SSW was detected by analyzing the time series of T_B fields over the southern polar region in late August–September 2019 at the O1–O10 channel frequencies (see Table I). Fig. 11 shows changes in the brightness temperature of the polar area acquired in channel O8 MTVZA-GY. T_B is proportional to air temperature of stratospheric layer between about 27 and 38 km. The T_B fields before the warming (25 August), at the beginning of warming (30 August–5 September), and during its evolution (10–30 September, 2019) are given in [31].

The satellite data agree with the vertical profiles of air temperature $T(h)$ from the radiosonde data released from the South Pole station 89009 and the Antarctica coastal stations 89062, 89055, 89592, 89611, 89664, and 89532 (Fig. 12). Fig. 12 shows the $T(h)$ profiles measured by radiosondes with the maximum ascent altitude. The positions of the stations are marked in Fig. 11(a) with white dots.

The brightness temperature of the Earth's outgoing radiation is determined only by atmospheric radiation at frequencies at which the integral absorption of the atmosphere on the line-of-sight $\tau = \tau_0 \times \sec\theta > 4$–5 Np where τ_0 is the total absorption in the nadir direction. The contribution of different layers of the atmosphere to the outgoing radiations is described by the weighting function WF(ν,h), which depends on air temperature, pressure, and humidity, as well as the gas composition.

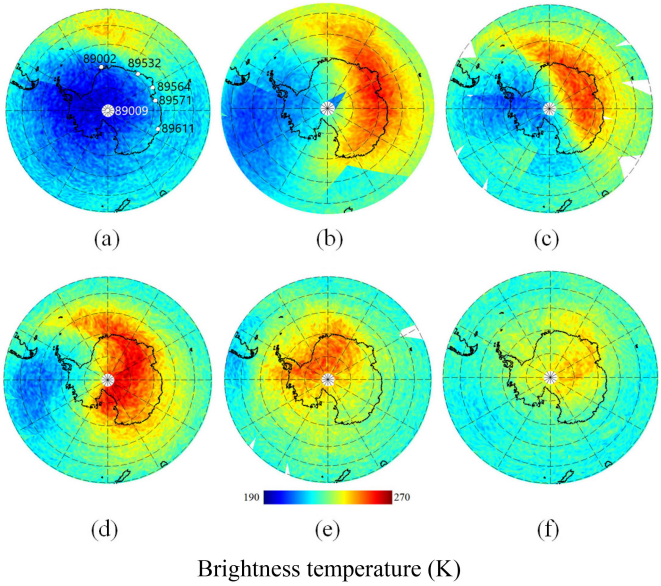

Fig. 11. Brightness temperature of the southern polar region in channel O8 showing the air temperature between about 27 and 38 km measured by Meteor-M No. 2-2 MTVZA-GY during SSW on (a) 25 and (b) 30 August and (c) 5, (d) 10, (e) 20, and (f) 30 September 2019. White dots in (a) mark the location of radiosonde stations in Antarctica. Digits near white dots are station's numbers.

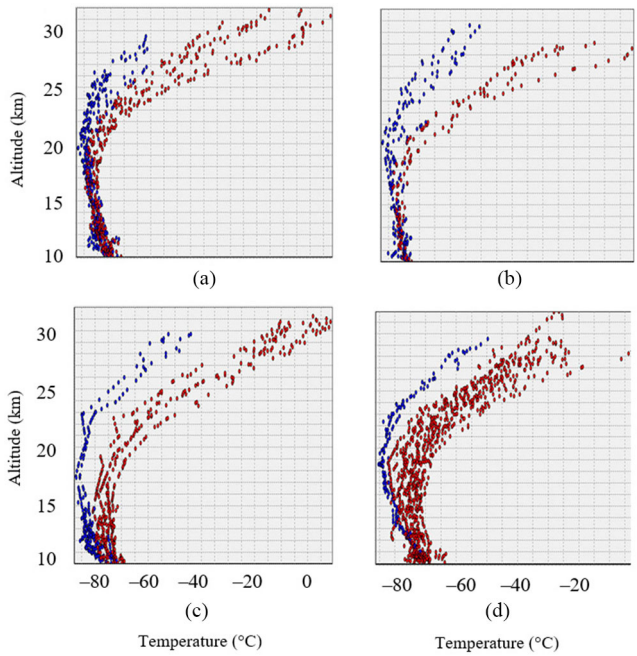

Fig. 12. Vertical profiles of air temperature measured by radiosondes released from stations. (a) 89532 Syowa on 21–26 (blue points) and 27–31 (red points) August, (b) 89567 Mawson on 21–26 (blue) and 27–31 August (red), (c) 89009 Amundsen-Scott on 1–8 (blue) and 9–20 (red) September, and (d) 89002 Neumaier on 1–4 (blue) and 5–30 (red) September 2019.

Weighting functions for O1–O10 channels shown in Fig. 13 were calculated using profiles of average temperature and average pressure in June–August in a latitude belt 65–75° S [11]. As the sounding frequency increases, the position of the maxima of the weighting function shifts in height. In channels O1–O3,

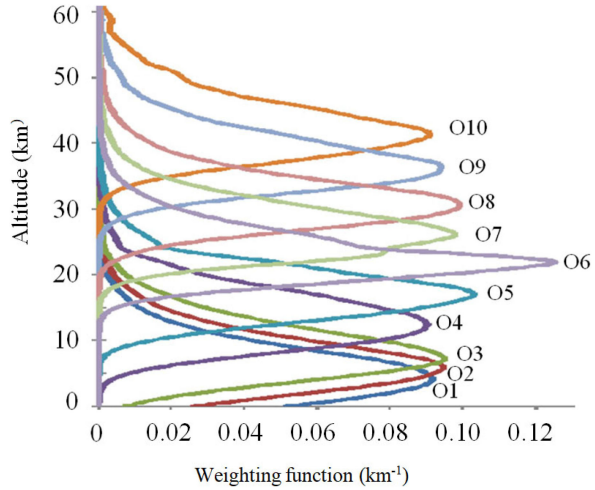

Fig. 13. Weighting functions at frequencies of channels O1–O10 in the range 52.8–57.8 GHz, calculated for the belt of latitude 65–75° S at an incidence angle of 65°. The numbers on the curves correspond to the channel designations in Table I.

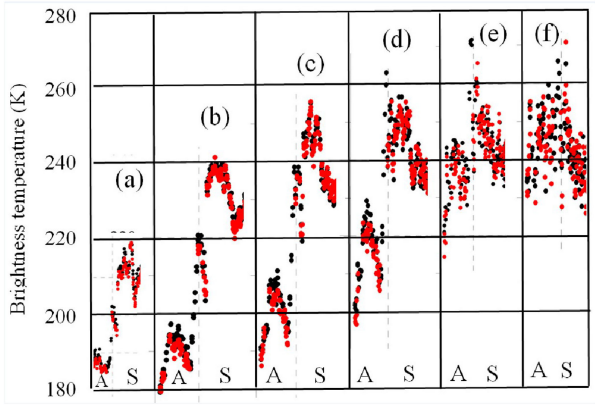

Fig. 14. Time series of the brightness temperatures on oxygen channels (a) O5, (b) O6, (c) O7, (d) O8, (e) O9, and (f) O10 measured by MTVZA-GY over Concordia station area since August 6 till September 30, 2019 at ascending (red dots) and descending (dark dots) orbits. A – August, S – September.

the maxima are located at height $h < 10$ km, and the received radiation is mainly formed in the troposphere. The WF maxima in channels O4–O10 are in the lower and middle stratosphere.

Ten frequencies in the area of the oxygen absorption band (channels O1–O10, Table I) are used for measuring the temperature of different layers of the troposphere and stratosphere and studying its spatial and temporal variability. The maximum altitude of most of the radiosondes launched from the Amundsen-Scott station and from stations on the coast of Antarctica did not exceed 28 km, which, combined with data gaps, and the rare network of radiosonde stations, does not allow us to study the dynamics of the phenomenon at different altitudes with good temporal resolution. The MTVZA-GY measurements over the entire Antarctica are performed at least twice a day, and over Amundsen-Scott and Concordia (75.5° S, 16.25° E) stations much more frequently.

The time series of $T_B(\nu)$ on channels O5–O10 (Fig. 14) give idea on development of warming for the period from August

6 to September 30, 2019 in different layers of the atmosphere, on sharp temporal gradients and maximum amplitudes of air temperature over one area in the Eastern Antarctica. The $T_B(\nu)$ values were obtained by averaging all pixels in a circle with a diameter of 200 km, centered at Concordia station.

Development of SSW in late August–September 2019 over the South Pole can be traced with confidence on the data of Merra-5 reanalysis. Analysis of these data shows that the SSW over Antarctica was caused by a quasi-six-day Rossby wave formed in the polar stratosphere at 30–40 km heights, where the atmosphere is unstable due to strong vertical wind drift associated with planetary wave collapse [32].

SSWs in the Northern Hemisphere were detected by MTVZA-GY from Meteor-M No. 2 in 2015–2016 [5] and from Meteor-M No. 2-2 in January 2021 [33]. The experience of MTVZA-GY data analysis during SSW in both Southern and Northern Hemispheres may be in demand along with MW measurements of other sensors and modeling data. The relevance of detailed SSW studies is due to the numerous connections of processes in the stratosphere with processes in the ionosphere [32] and troposphere [34]–[38].

VI. Discussion and Conclusion

The global brightness temperature fields obtained simultaneously in a wide frequency range by MTVZA-GY MW radiometer allow us to carry out the combined study of Earth's ocean–atmosphere–land system, visualize the spatial structure of natural phenomena and processes on the underlying surface and in the subsurface layer (Antarctica and Greenland ice sheets), in the troposphere and stratosphere. Now in November 2021 (at the time of the revision of the article), more than two years after the Meteor-M No. 2-2 launch MTVZA-GY is performing nominally and continues to collect global data on our planet as follows from Figs. 5 to 9 and papers [1], [31], [33].

MTVZA-GY scans the Earth at an incidence angle $\theta = 65°$ in contrast to AMSR2 and GMI radiometers, where $\theta = 53$–$55°$. As a result, the contribution of upwelling $T_B{}^{\uparrow}(\nu)$ and downwelling $T_B{}^{\downarrow}(\nu)$ components of the brightness temperature of the atmosphere to the brightness temperature $T_B(\nu)$ measured by the satellite increases, while the contribution of underlying surface radiation decreases. The total contribution of the atmosphere $T_{B\mathrm{atm}}(\nu)$ can be presented in the form of $T_{B\mathrm{atm}}(\nu) = T_B{}^{\uparrow} + T_B{}^{\downarrow} \times [(1-\kappa(\nu)] \times \mathrm{e}^{-\tau 0^{(\nu)\sec\theta}}$. At $\theta = 65°$, the emissivity of the ocean surface in horizontal polarization $\kappa^H(\nu)$ is less than at $\theta = 53$–$55°$, which also leads to an increase in the contribution of the atmosphere emission to $T_B(\nu)$.

Variations in total absorption $\tau(\nu) = \tau_0(\nu)\sec\theta$ and brightness temperature of the atmosphere $T_{B\mathrm{atm}}(\nu)$ along the sensing direction are due to variations in atmospheric water vapor content V, cloud liquid water content Q, and liquid and solid precipitation. The derivatives of $T_B(\nu)$ by parameters are maximal at small values of V and Q. From the simulation results, for example, it follows that the T_B increment at $\nu = 23.8$ GHz caused by a cloud with $Q = 0.06$ kg/m^2 against a clear sky background is $\approx$5 K at $\theta = 65°$ and $\approx$3.5 K at $\theta = 55°$ (SST $\approx$ 2 °C, cloud droplet temperature $t_{\mathrm{cl}} = -5$ °C, total water vapor content $V \approx 6$ kg/m^2, and wind speed $W = 5$ m/s). At frequency 36.5 GHz, which is commonly used in many algorithms for retrieval of cloud liquid water content, the T_B increment is $\approx$10 K and $\approx$7 K, respectively.

A wide swath of MTVZA-GY radiometer ($L = 2500$ km) due to the incidence angle $\theta = 65°$ significantly increases the possibilities of studying the dynamics of the ice cover. It follows from a comparison of AMSR2 measurements ($L = 1450$ km) with the model data of the Copernicus Imaging Microwave Radiometer (CIMR) ($L > 1900$ km). It is shown that processing the data obtained on consecutive CIMR swaths ("swath-to-swath" approach) allows increasing the number of retrieved sea ice drift vectors by about two orders of magnitude more than using the daily T_B fields from AMSR2 data [39].

With a swath width of 2500 km, the gain can be even greater, both for the sea ice cover and for dynamic atmospheric processes such as polar lows. If the atmospheric formations are on overlapping parts of two consecutive orbits, it is possible to determine their average displacement rate and estimate the variability of the parameters V, Q, and W derived from $T_B(\nu)$ over the time between observations. This information is needed for monitoring and nowcasting. Especially, promising is the use of data obtained by the joint analysis of MTVZA-GY, AMSR2, and GMI measurements. For this purpose, the spatial resolution of the MTVZA-GY data at frequencies $\nu = 10.7$, 18.7, and 36.5 GHz, should be approximated to that of AMSR2 and CIMR (15, 5, and $<$5 km) resolution, respectively. The effectiveness of the approach can also be evaluated by comparing the available MTVZA-GY and AMSR2 data acquired over the Norwegian and Barents Seas.

The relative decrease in the contribution of ocean radiation to $T_B(\nu)$ at $\theta = 65°$ leads to the increase in the error of the retrieved wind speed. The error increases with increasing cloud water content and atmospheric water vapor content. Therefore, the advantages of the 65-degree angle of incidence are most noticeable when applying MTVZA-GY data for the study of ocean–atmosphere system in polar and temperate latitudes of both hemispheres.

At tropical and subtropical latitudes and in extratropical cyclones, V and Q values and precipitation intensity increase significantly. The joint analysis of MTVZA-GY data at frequencies from 10 to 183 GHz and close-time infrared images makes it possible to distinguish thick rain-producing clouds from other cloud forms. At $\nu < 50$ GHz, the absorption in droplet clouds and their brightness temperature increases with decreasing droplet temperature and with increasing frequency while Q is constant (Figs. 6 and 7). At frequencies in the 90 GHz region and in the 176–190 GHz water vapor resonance region, thick convective clouds can have both positive and negative T_B contrasts to the surrounding background (Fig. 8). It follows from the results of simulations of MW radiation transfer in the cloud atmosphere above the ocean [40] and analysis of satellite data that the amplitude and sign of the $T_B(\nu)$ increment, besides frequency and polarization, depend on the temperature and phase (liquid or solid) of cloud particles, their size distribution, and on the vertical profiles of atmospheric temperature and humidity.

Areas with deep convection appear in the brightness temperature fields in the form of spots and extended elongated

formations with decreased $T_B(\nu)$ values at high frequencies and with increased $T_B(\nu)$ values at low frequencies. The decrease or increase of $T_B(\nu)$ is determined by the processes of scattering and absorption of radiation in the medium consisting of water and/or ice particles of different sizes and shapes. Precipitation over the ocean and land is clearly visible in the T_B fields at $\nu = 91.6$ GHz and 183 ± 7 GHz not only in the ITCZ and in the tropical regions of South America and Africa (Fig. 8) but also in the atmospheric fronts, extratropical cyclones, and atmospheric rivers, which follows from the comparison of Fig. 8 with Figs. 6 and 7.

The pronounced spatial heterogeneity of the water vapor distribution and its height distribution manifests itself in the brightness temperature fields in the water vapor channels. Strong absorption in water vapor in these channels visualizes the structure of cyclones; position of atmospheric fronts; areas of heavy clouds; and precipitation over the ocean, sea ice, and land, which follows from comparison of the T_B field at 183.31 ± 1.4 GHz [see Fig. 8(b)] with the T_B fields at imager frequencies [see Figs. 5–8(a)]. The experimental T_B signatures are in agreement with simulation data.

The time series of brightness temperatures in the imager and water vapor channels help to monitor and interpret surface and atmospheric signatures in the remote polar regions caused by changes in the sea and land ice surface conditions (dry or wet), in location and structure of cyclones (Figs. 9 and 10). The analysis of the time series of brightness temperatures in water vapor channels HO1, HO2, and HO3 (see Table I) shows that at $V > 3$ kg/m^2, surface radiation can be neglected, and the variability of T_B is related to changes in the vertical profiles of air temperature and humidity. Increments of T_B over the Concordia station in East Antarctica reached 50–70 K over several days during cold seasons 2019–2020 and 2020–2021 when relatively warm and moist air was observed by radiosondes issued from the Antarctic coast and the South Pole [their locations seen in Fig. 11(a)].

The analysis of daily $T_B(\nu)$ images of the southern polar region obtained by MTVZA-GY in August–September 2019 at ten frequencies in the oxygen absorption band (channels O1–O10, Table I) showed the development of SSW over Antarctica (Figs. 11 and 14) [31]. The SSW was confirmed by the air temperature profiles obtained with radiosondes (Fig. 12) and the works mainly based on modeling and reanalysis data [32], [41], [42].

Sudden warming events in the stratosphere of the Northern Hemisphere were recorded by MTVZA-GY in 2015–2016 with Meteor-M No. 2 [5] and in January 2021 with Meteor-M No. 2-2 [33]. SSWs have a large-scale influence on atmospheric circulation, ozone distribution, air temperature, and precipitation anomalies covering entire continents. According to the studies [35]–[38], [42], they serve as a reliable predictor of large-scale weather anomalies. Daily global MTVZA-GY measurements are thus a valuable source of information on stratospheric air temperature.

The $T_B(\nu)$ fields were constructed from external calibration data based on numerical integration of the MW radiative transfer equation over selected cloudless hot and cold test zones, for which the surface temperature and emissivities and vertical profiles of atmospheric temperature and humidity were known. The parameters of the underlying surface and atmosphere are subject to diurnal, synoptic, and seasonal changes, which affect the calculated values of brightness temperatures and the coefficients of the regression equations used for the transition from counts to T_B (even if the instrument is stable in space). Therefore, if the mentioned conditions over the test zones are observed, the external calibration should be carried out during the whole period of radiometer operation and more often during the flight test phase [43]. Obtaining quantitative information on geophysical parameters and monitoring the performance of the radiometer in flight depend on the accuracy of internal calibration and external calibration and results of numerical modeling of brightness temperatures.

The MTVZA-GY data can be used both in the operational mode in the organizations of Ministry of Emergencies and Roskomgidromet and in studying the regional and global climate variability. The most important tasks for the nearest future are the following: Evaluation of variability of calibration coefficients and stability of MTVZA-GY operation in space, development, and improvement of algorithms for geophysical parameter retrieval taking into account the experience accumulated during processing of MW data acquired by Meteor-M No. 2 and 2-2. Next meteorological satellites with onboard MTVZA-GY radiometer are planned to launch in 2022 and 2023.

REFERENCES

[1] G. M. Chernyavskii, L. M. Mitnik, V. P. Kuleshov, M. L. Mitnik, M. A. Strel'tsov, I. V. Evseev, and I. V. Cherny, "Brightness temperature modeling and first results derived from the MTVZA-GY radiometer of the Meteor-M No. 2-2 satellite," *Curr. Problems Remote Sens. Earth From Space*, vol. 17, no. 3, pp. 51–65, 2020.

[2] L. Mitnik, V. Kuleshov, M. Mitnik, A.M. Streltsov, G. Cherniavsky, and I. Cherny, "Microwave scanner sounder MTVZA-GY on new Russian meteorological satellite Meteor-M N 2: Modeling, calibration and measurements," *IEEE J. Sel. Topics Appl. Earth Observ. Remote Sens.*, vol. 10, pp. 3036–3045, Jul. 2017.

[3] G. M. Cherniavsky, L. M. Mitnik, V. P. Kuleshov, M. L. Mitnik, and I. V. Cherny, "Microwave sensing of the ocean, atmosphere and land surface from Meteor-M No. 2 data," *Curr. Problems Remote Sens. Earth From Space*, vol. 15, no. 4, pp. 78–100, 2018, doi: 10.21046/2070-7401-2018-15-4-78-100.

[4] L. M. Mitnik, V. P. Kuleshov, M. L. Mitnik, and A.V. Baranyuk, "Passive microwave observations of South America and surrounding oceans from Russian Meteor-M no. 2 and Japan GCOM-W1 satellites," *Intern. J. Remote Sens.*, vol. 39, no. 13, pp. 4513–4530, 2018.

[5] L. M. Mitnik, V. P. Kuleshov, M. K. Pichugin, and M. L. Mitnik, "Sudden stratospheric warming in 2015-2016: Study with satellite passive microwave data and reanalysis," *Proc. IEEE Int. Geosci. Remote Sens. Symp.*, Jul. 2018, pp. 5560–5563.

[6] T. Meissner and F. J. Wentz, "The complex dielectric constant of pure and sea water from microwave satellite observations," *IEEE Trans. Geosci. Remote Sens.*, vol. 42, no. 9, pp. 1836–1849, Sep. 2004.

[7] T. Meissner and F. J. Wentz, "The emissivity of the ocean surface between 6 and 90 GHz over a large range of wind speeds and earth incidence angles," *IEEE Trans. Geosci. Remote Sens.*, vol. 50, no. 8, pp. 3004–3026, Aug. 2012.

[8] S. Prakash, H. Norouzi, M. Azarderakhsh, R. Blake, C. Prigent, and R. Khanbilvardi, "Estimation of consistent global microwave land surface emissivity from AMSR-E and AMSR2 observations," *Appl. Meteorol. Climatol.*, vol. 57, pp. 907–919, 2018.

[9] L. M. Mitnik and M. L. Mitnik, "Retrieval of atmospheric and ocean surface parameters from ADEOS-II AMSR data: Comparison of errors of global and regional algorithms," *Radio Sci.*, vol. 38, no. 4, 2003, Art. no. 8065.

[10] Wyoming. [Online]. Available: http://weather.uwyo.edu/upperair/sounding.html

[11] "Global reference atmosphere for altitudes from 0 to 120 km for aerospace practice," (in Russian), GOST P 53460-2009, p. 253, 2009.

[12] H. Amit, F. Terra-Nova, M. Lézin, and R. I. Trindsde, "Non-monotonic growth and motion of the South Atlantic Anomaly," *Earth Planets Space*, vol. 73, no. 38, 2021, Art. no. 10. [Online]. Available: https://doi.org/10.1186/s40623-021-01356-w

[13] X. Zou and X. Tian, "Striping noise analysis and mitigation for microwave temperature sounder-2 observations," *Adv. Atmos. Sci.*, vol. 36, no. 7, pp. 711–720, 2019.

[14] L. M. Mitnik, M. L. Mitnik, and E. V. Zabolotskikh, "Microwave sensing of the atmosphere-ocean system with ADEOS-II AMSR and aqua AMSR-E," *J. Remote Sens. Soc. Jpn.*, vol. 29, no. 1, pp. 156–165, 2009.

[15] L. P. Bobylev, E. V. Zabolotskikh, L. M. Mitnik, and M. L. Mitnik, "Atmospheric water vapor and cloud liquid water retrieval over the Arctic Ocean using satellite passive microwave sensing," *IEEE Trans.Geosci. Remote Sens.*, vol. 49, no. 1, pp. 283–294, Jan. 2010.

[16] L. M. Mitnik and M. L. Mitnik, "Algorithm for sea surface wind retrieval in tropics from AMSR-E data and its application to analysis of weather systems," *Investigation Earth From Space*, no. 6, pp. 34–44, 2011.

[17] E. V. Zabolotskikh, L. M. Mitnik, and B. Chapron, "New approach for severe marine weather study using satellite passive microwave sensing," *Geophys. Res. Lett.*, vol. 40, no. 13, pp. 3347–3350, 2013.

[18] L. M. Mitnik and M. L. Mitnik, "Calibratrion and validation are required components of microwave radiometric measurements from Meteor-M series satellites," *Curr. Problems Remote Sens. Earth From Space*, vol. 13, no. 1, pp. 95–104, 2016.

[19] D. T. Eppler *et al.*, "Passive microwave signatures of sea ice," in *Microwave Remote Sensing of Sea Ice*, F. Carsey, Ed. Washington, DC, USA: Amer. Geophys. Union, 1992, pp. 47–71.

[20] N. Mathew, G. Heygster, and C. Melsheimer, "Surface emissivity of the Arctic sea ice at AMSR-E frequencies," *IEEE Trans. Geosci. Remote Sens.*, vol. 47, no. 12, pp. 4115–4124, Dec. 2009.

[21] D. P. Schneider and E. J. Stei, "Spatial and temporal variability of Antarctic ice sheet microwave brightness temperatures," *Geophys. Res. Lett.*, vol. 29, no. 20, 2002, pp. 25–21–25–4, doi: 10.1029/2002GL015490.

[22] G. Macelloni, M. Brogioni, P. Pampaloni, and A. Cagnati, "Multifrequency microwave emission from the East Antarctic Plateau: Temporal and spatial variability," *IEEE Trans. Geosci. Remote Sens.*, vol. 45, no. 7–1, pp. 2029–2039, Jul. 2007.

[23] P. S. Narvekar, G. Heygster, T. J. Jackson, R. Bindlish, G. Macelloni, and J. Notholt, "Passive polarimetric microwave signatures observed over Antarctica," *IEEE Trans. Geosci. Remote Sens.*, vol. 48, no. 3, pp. 1059–1075, Mar. 2010.

[24] S. Surdyk, "Using microwave brightness temperature to detect short-term surface air temperature changes in Antarctica: An analytical approach," *Remote Sens. Environ.*, vol. 80, no. 2, pp. 256–271, 2002.

[25] I. P. Mazin and A. K. Khrgian, Eds. *Clouds and Cloudy Atmosphere: Handbook*, (in Russian). Leningrad, Russia: Hydrometeoizdat, 1989, pp. 1–646.

[26] F. M. Ralph *et al.*, "Atmospheric rivers emerge as a global science and application focus," *Bull. Amer. Meteorol. Soc.*, vol. 98, no. 9, pp. 1969–1973, 2017.

[27] I. V. Gorodetskaya, M. Tsukernik, K. Claes, M. F. Ralph, W. D. Neff, and N. P. M. van Lipzig, "The role of atmospheric rivers in anomalous snow accumulation in East Antarctica," *Geophys. Res. Lett.*, vol. 41, no. 17. pp. 6199−6206, 2014. [Online]. Available: https://doi.org/10.1002/2014GL060881

[28] L. Liang, L. Xinwu, and F. Zheng, "Spatio-temporal analysis of ice sheet snowmelt in Antarctica and Greenland using microwave radiometer data," *Remote Sens.*, vol. 11, no. 1838, 2019, Art. no. 13.

[29] A. H. Butler, J. P. Sjoberg, D. J. Seidel, and K. H. Rosenlof, "A sudden stratospheric warming compendium," *Earth Syst. Sci. Data*, vol. 9, no. 1, pp. 63–76, 2017, doi: 10.5194/essd-9-63-201.

[30] M. P. Baldwin *et al.,* "Sudden stratospheric warmings," *Rev. Geophys.*, vol. 59, no. 1, 2021, Art. no. e2020RG000708.

[31] L. M. Mitnik, V. P. Kuleshov, and M. L. Mitnik, "Sudden stratospheric warming over Antarctica in September 2019 from Meteor-M No. 2-2 MTVZA-GY radiometer," *Curr. Problems Remote Sens. Earth From Space*, vol. 17, no. 7, pp. 229–242, 2020, doi: 10.21046/2070-7401-2020-17.

[32] Y. Yamazaki *et al.*, "September 2019 Antarctic sudden stratospheric warming: Quasi-6-day wave burst and ionospheric effects," *Geophys. Res. Lett.*, vol. 47, 2020, Art. no. e2019GL086577. [Online]. Available: https://doi.org/10.1029/2019GL086577

[33] L. M. Mitnik, V. P. Kuleshov, and M. L. Mitnik, "Sudden stratospheric warming in January 2021 by microwave measurements from Meteor-M No. 2-2 satellite," *Curr. Problems Remote Sens. Earth From Space*, vol. 18, no. 3, pp. 139–148, 2021.

[34] N. M. Pedatella *et al.*, "How sudden stratospheric warming affects the whole atmosphere," *EOS*, vol. 99, 2018. [Online]. Available: https://doi.org/10.1029/2018EO092441

[35] A. D. King, A. H. Butler, M. Jucker, N. O. Earl, and I. Rudeva, "Observed relationships between sudden stratospheric warmings and European climate extremes, "*J. Geophys. Res. Atmos.*, vol. 124, no. 13, pp. 13943–13961, 2019.

[36] H. Afargan-Gerstman and D. I. V. Domeisen, "Pacific modulation of the North Atlantic storm track response to sudden stratospheric warming events," *Geophys. Res. Lett.*, vol. 47, no. 2, 2020, Art. no. e2019GL085007.

[37] D. I. V. Domeisen and A. H. Butler, "Stratospheric drivers of extreme events at the Earth's surface," *Commun. Earth Environ.*, vol. 1, no. 59, 2020. [Online]. Available: https://doi.org/10.1038/s43247-020-00060-z

[38] R. J. Hall, D. M. Mitchell, W. J. M. Seviourand, and C. J. Wright, "Tracking the stratosphere-to-surface impact of sudden stratospheric warmings," *J. Geophys. Res. Atmos.*, vol. 126, no. 3, 2021, Art. no. e2020JD033881, doi: 10.1029/2020JD033881.

[39] T. Lavergne, M. Piñol Solé, E. Dow, and C. Donlon, "Towards a swath-to-swath sea-ice drift product for the Copernicus Imaging Microwave Radiometer mission," *Cryosphere*, vol. 15, pp. 3681–3698, 2021. [Online]. Available: https://doi.org/10.5194/tc-15-3681-2021

[40] R. Chen and R. Bennarz, "Sensitivity of 89–190-GHz microwave observations to ice particle scattering," *J. Appl. Meteor. Climatol.*, vol. 59, no. 7, pp. 1195–1215, 2020. [Online]. Available: https://doi.org/10.1175/JAMC-D-19-0293.1

[41] J. Rao, C. I. Garfinkel, I. P. White, and C. Schwartz, "The Southern Hemisphere sudden stratospheric warming in September 2019 and its predictions in S2S models," *J. Geophys. Res. Atmos.*, vol. 125, no. 14, 2020, Art. no. e2020JD032723. [Online]. Available: https://doi.org/10.1029/2020JD032723

[42] E.-P. Lim *et al.*, "The 2019 Southern Hemisphere stratospheric polar vortex weakening and its impact," *Bull. Amer. Meteorol. Soc.*, vol. 102, no. 6, 2021. [Online]. Available: https://doi.org/10.1175/BAMS-D-20-0112.1

[43] K. J. Coakley, J. Splett, D. Walker, M. Aksoy, and P. Racette, "Microwave radiometer instability due to infrequent calibration," *IEEE J. Sel. Topics Appl. Earth Observ. Remote Sens.*, vol. 13, pp. 3281–3290, Apr. 2020, doi: 10.1109/JSTARS.2020.2984004.